DRAG, LIFT AND PITCHING MOMENT INCREMENTS DUE TO WIND TUNNEL WALL CONSTRAINT: EXTENSION TO THREE DIMENSIONS

J. E. Hackett[1], K. R. Cooper[2], M. L. Perry[1]

Abstract

Wind-tunnel-induced flow distortion around a test model causes drag, lift and pitching moment increments that are absent in free air. Previous two-dimensional predictions of these effects are extended to three dimensions and means for evaluating them are discussed. A new extension to Maskell's blockage prediction method, designated "Maskell III", is introduced that estimates the lift increment. Other boundary correction approaches include procedures based on the use of wall pressure measurements and the application of pressure signature and two-variable algorithms. These studies are supported by dedicated experiments on a family of flat plate wings, carried out at the NRC. Initial applications of the new correction methods to these data have produced encouraging results.

Nomenclature

b	model span.
B	tunnel width.
c	wing mean chord.
c_S	spacing of solid blockage source-sink pair.
C	tunnel cross sectional area, B x H.
C_D, C_L, C_M	wind-axis drag, lift and pitching moment coefficients.
ΔC_D,ΔC_L,ΔC_M	increments in C_D, C_L, C_M caused by tunnel induced velocity gradients, to be subtracted from measured data.
H	tunnel height.
q, Δq	dynamic pressure and its change due to tunnel effects.
$+Q_S$, Q_W, $-Q_S$	solid blockage source, wake source and solid blockage sink strengths.(L^2/T)
S	model reference area.
U_0	mainstream velocity, far upstream.
u, v	interference velocities in the X and Y directions.
x, y, z	Tunnel co-ordinates. Streamwise, normal to chord and spanwise for the present half model.
α, $\Delta\alpha$	angle of attack and its change due to tunnel effects.
δ	upwash interference velocity, v, normalized on U_0.
Γ_T	strength of lifting vortex.(L^2/T)
$+\Delta\Gamma$, $-\Delta\Gamma$	strengths of pitching moment vortices.(L^2/T)
ε	blockage interference velocity, u, normalized on U_0.
η	proportion of model chord.
κ	scaling factor for lift-dependent pitching moment.
ρ	fluid mass density.

Subscripts:

1, 2, 3	at locations (x_1, y_1)..... (x_3, y_3) (see [10]).
c	corrected.
i	index for sensing points.
j	index for singularities.
L	due to lift image or image set.
M	due to pitching moment image or image set.
N	normal to chord.
S	due to solid body image or image set.
T	total.
u	uncorrected.
vis	associated with viscous drag.
W	due to wake source image or image set.
Wds	due to downstream wake sink.

[1] Lockheed Martin Aeronautics Company, Marietta, Georgia, USA
[2] National Research Council, Ottawa, Canada.

Copyright ©2000 by J.E.Hackett. Published by the International Council of the Aeronautical Science with permission.

1 Introduction

The greatly expanded flight envelope of modern, super-maneuverable fighters has presented new challenges in low-speed wind tunnel testing. Controlled flight is now possible at very high angles of attack, aided by thrust vectoring. Both features increase the difficulties in estimating tunnel effects. Rig constraints can add to the challenge. At angles beyond about 45 degrees, for example, there may be no option but to allow a model mounted on a conventional sting to move upward in the test section toward the roof. The consequent need to provide corrections for off-center conditions further compounds the problem because cross interactions arise between force components.

Contemporaneously, there have been significant advances in methods for estimating tunnel boundary induced velocities. These have the potential to mitigate the problem, but translating tunnel-induced velocity increments into model force corrections remains a major hurdle. The present paper will review recent progress made by the authors towards estimating tunnel induced interference forces and moments for both on-center and off-center models, with emphasis on velocity gradient effects.

Dedicated tests were carried out on a family of semi-span flat plate wings in an NRC wind tunnel (see Section 2 below and [1]). Extensive balance and wall pressure measurements were made over ranges of angle of attack, model size and off-center location. These data are available, on request, from the second author.

Wall pressures were analyzed using the two-variable method [2], as implemented by Mokry [3], and other methods. Figure 1 shows estimated interference data for an aspect ratio three flat plate wing, centered in the tunnel, at 10, 60 and 90 degrees angle of attack. The model plan area, at 16% of the test section area, was the largest tested. The upper and lower plots in Figure 1 show distributions of tunnel-induced dynamic pressure and angle of attack effects near the x-axis. Each sub-plot includes data ahead of the model, at mid chord and behind the model. It is evident that both the interference itself and its gradients can be significant.

The three angles of attack selected for Figure 1 were chosen to represent three flow regimes of interest. At ten degrees, the angle of attack correction and its gradient are significant. However the flow is unseparated and blockage corrections are small. The converse is true at ninety degrees: the blockage is large but there is no lift, and so there is no tunnel-induced angle of attack for this centered condition. The intermediate case, at sixty degrees, represents a serious challenge because both gradient and angle of attack effects are large. The fact that the model may approach the tunnel roof at this point - for rig reasons - adds to the challenge.

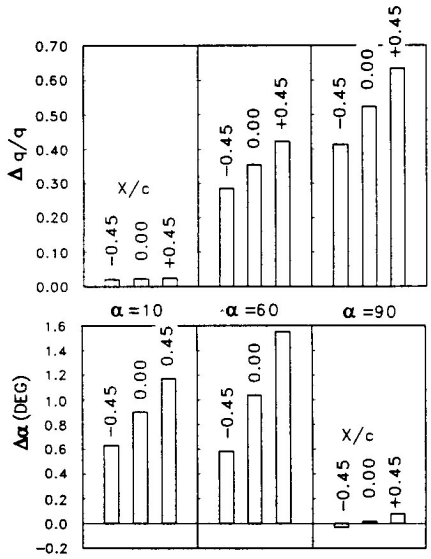

Figure 1 Interference and interference gradients at (X, 0, 0) for a flat plate wing.

There are several options for defining changes in the model flow environment caused by the tunnel. Long-standing classical methods have little difficulty with attached-flow cases and small models, but cannot accommodate fully separated flows, particularly when there is significant lift or when tunnel effects modify the shape of a separation bubble. Wall pressure measurements reflect not only the forces on the model but also the nature of the flow around it [4]. The onus is on interpreting these pressures properly. This problem has been solved for low-

lift, fully separated flows, such as the normal flat plate, and the ability to deal with tunnel-induced shrinkage of the separation bubble has been demonstrated in [5]. Bubble changes are also accommodated by the earlier method of Maskell [6] which recognizes the linkages to viscous drag and base pressure. His procedure has recently been modified [5,7] to separate the contributions of the drag increment, ΔC_D, and dynamic pressure. A further extension, that we designate "Maskell III", described in Section 3, finds the corresponding value of ΔC_L for inclined, stalled plates.

Having defined the tunnel-induced changes in flow environment, a theoretical flow model is required that can capture the essential far-field flow features without undue complication. Available methods range from the three-source, three-vortex model of the augmented pressure signature method, in [8], to elaborate paneling schemes such as those of [9].The findings of [10] demonstrate the dangers of using a particular flow model inappropriately. An attempt was made to model a 2D symmetrical airfoil with fully attached flow using a three-source, three-vortex system. Four unknown singularity strengths were found using lift, drag, pitching moment and model thickness information, without reference to the boundary conditions on the model itself. When the model was moved close to the 2D tunnel roof it was found that a highly cambered body was implied that carried the correct loads but experienced interference forces that were far too small. An approach with a good track record for separated flows failed when applied to an attached flow case.

A flow model is required that can accommodate both fully attached flow and the highly separated, lifting conditions of the 60 degree case cited above. The normal flow boundary condition must be satisfied on at least the model's front face and the ability to model a separated wake must be included. Means for meeting these goals will be discussed in Section 3.

Section 4 will discuss the practical details of implementing the three schemes discussed above. Limited applications of these methods to the new, flat plate wing data will be described in Section 5, leading to discussion in Section 6 and conclusions in Section 7.

2 Experiments on flat plate wings

The four flat-plate, refection-plane wing models could be mounted on a six component balance and turntable assembly situated below the floor of the pilot wind tunnel at the NRC Aerodynamics Laboratory. This closed-return tunnel has a 0.914m x 0.914m x 2.25m test section and a maximum speed of 55m/s. It has flow angle variations of less than 0.2 degrees and dynamic-pressure non-uniformity of less than 0.5% over the test area. The balance had a measurement range in lift and drag of 50lb and a measuring accuracy of 0.1%.

The models, which had a full-span aspect ratio of three, were geometrically scaled in all respects, including span, chord, thickness, edge bevel, mounting strut geometry and root-sealing arrangements. Two models and the tunnel principal dimensions are sketched in Figure 2. All models had chord/span/thickness in the ratios 1.0/1.5/0.032, respectively, with area blockages, (S/C), of 0.040, 0.071, 0.111 and 0.160. The model-support assembly was located on a set of linear bearings that allowed it to traverse across the width of the wind tunnel. This moved the half-model's lifting surface towards the right wall, looking upstream.

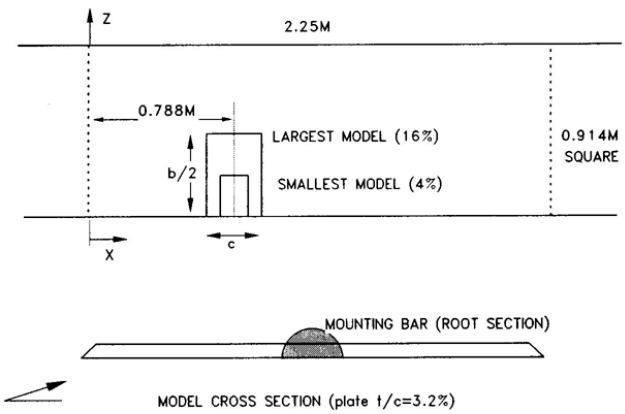

Figure 2 Tunnel and model dimensions

The models were positioned 0.788m downstream of the entrance to the test section and were tested at up to six locations across the tunnel at fixed non-dimensional distances measured from the side wall of (y/c) = (0.72, 0.88, 1.22, 1.72, 2.22, on center). The first three and the last locations were common to all models. Each model was pitched about 50% chord at 26 angles from -5 to 110 degrees at an uncorrected speed of 30 m/s. This speed was chosen to ensure adequate pressure signals at the walls for all models. A series of preliminary runs performed with the largest model showed that Reynolds number was not a significant parameter. Other trial runs, varying tunnel floor boundary layer thickness, demonstrated that the best treatment was none. The presence of significant edge bevels on the wing upper surfaces and the tapered mounting bars (Figure 2) resulted in a model with positive camber, giving positive lift at zero incidence.

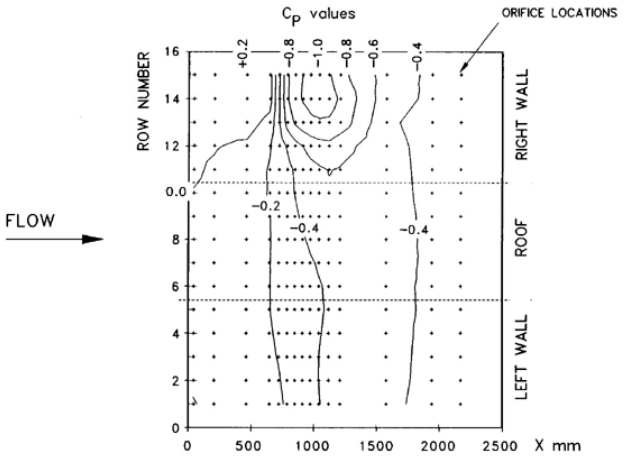

Figure 3 Tunnel surface pressures for large wing (S/C=0.16) at α = 50-deg, located 0.717 chords from the right wall

Flush-mounted aluminum bars were positioned in the tunnel walls with pressure orifices drilled into them. 240 pressure taps were distributed over 15 rows on the three instrumented walls. Each central row contained 20 taps for use with the pressure-signature method while the off-center rows contained 15 taps. Fifteen rows of 15 taps, shown in Figure 3, were used with the two-variable method. The pressure contours are for the largest model placed with its lifting surface 0.717 chords from the tunnel sidewall at 50 degrees angle of attack. A suction peak is evident opposite to the wing's lifting surface. A positive pressure peak, ahead of this, reflects the front stagnation. The fact that all the downstream C_P's asymptote to approximately minus 0.4 is a consequence of the model's large viscous blockage.

The left hand plots in Figure 4 show lift and drag measured at tunnel center for all four wings. All their stall characteristics are very similar- a consequence of the use of sharp-edged plates. Post- stall, there is a significant increase in lift and drag with plate size. The right hand plots in Figure 4 show the corresponding data with each model 0.717 chords from the right wall. It is apparent that the maximum lift has increased slightly and the spreads between plate sizes are less, especially for lift. Figure 5 shows cross plots against position in the tunnel for α = 50 degrees. A decrease in both lift and drag is seen at fixed angle of attack for the larger models as their upper surfaces approach the tunnel boundary. Instrumentation difficulties experienced with the pitching moment measurements have not yet been resolved so these data will not be presented here.

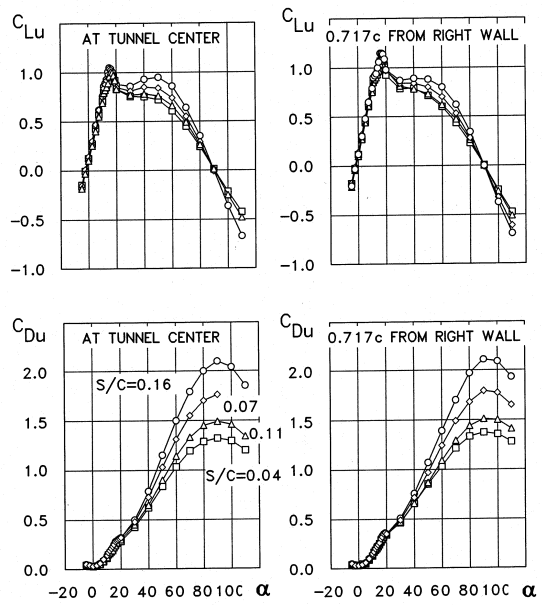

Figure 4 Typical data sets from the NRC flat flat plate wing tests

Data like those of Figure 3 were input to a two-variable interference program [3] to

determine tunnel-induced velocities at the model reference point and other locations. Figure 6 shows interference velocities at the reference point for the largest and smallest models at two locations. The two left plots show u- and v-component interference velocities at tunnel center and at 0.717 model chords from the right tunnel wall. Below stall, at approximately 16-deg, moving the large model from tunnel center towards the wall (+ versus x symbols) has a large effect on the u-component interference, but little effect on the v-component. At large angles of attack, the maximum u-interference is the same at both positions and the maximum v-interference increases by about 25%. At the same non-dimensional distance from the wall, normalized by chord, the smaller models are more sensitive to wall proximity then the larger models. This occurs because the smaller models are non-dimensionally more distant from the other three walls, reducing their alleviating effects.

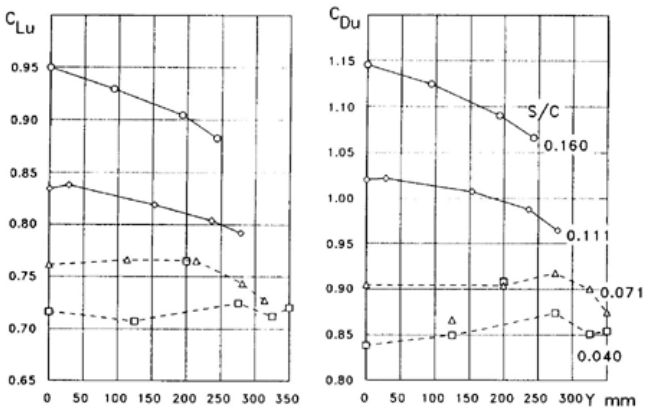

Figure 5 Effect of model position and size on uncorrected lift and drag at α = 50

The right side of Figure 6 show normal-to-chord velocity V_N and its gradient in the chordwise direction, calculated using the two-variable method. The worst case for along-chord normal velocity gradient (tunnel-induced camber) is at 60 degrees angle of attack for all of the configurations shown. There is negligible chordwise gradient for the small model on the tunnel centerline but a significant increase occurs next to the wall. The V_N gradient is likely to determine the correctability of any given data set, rather than V_N itself. Aft-stalling and high lift airfoils are the most susceptible.

3 Alternative flow models

The present approach to calculating tunnel interference increments rests on three basic premises. Firstly, the flow model used should be readily implemented with minimal model geometry details. Secondly, it should blend the most successful features of attached and fully-separated flow models. Thirdly, it is preferable that the transition from pre- to post-stall conditions be continuous with minimal user intervention.

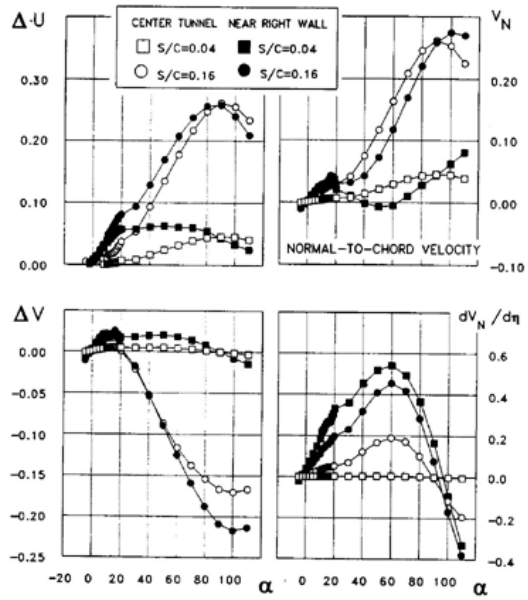

Figure 6 Interference velocities at the model reference point, using the two-variable method

As mentioned in the introduction, both attached flows and fully-separated, non-lifting flows can already be treated successfully. Attached flow cases can be simulated, assuming potential flow, by using vortex lattice or panel methods. Pressure signature methods, in various incarnations, have long been able to reproduce the essential features of fully-separated, non-lifting flows. The upper part of Figure 7 shows the geometry for the pressure signature method. The example selected is for the largest test wing of Section 2 placed at 90 degrees angle of attack at tunnel center. The three circle symbols

represent singularity locations (three sources and three vortices) found by the pressure signature method. The solid blockage source and sink, $\pm Q_S$, would generate a closed bubble but the wake source, Q_W, prevents this. It can be seen, in the lower part of Figure 7, that c_S, the source-sink spacing, decreases slightly with decreasing angle of attack, indicating a reduction of the (unclosed) bubble length.

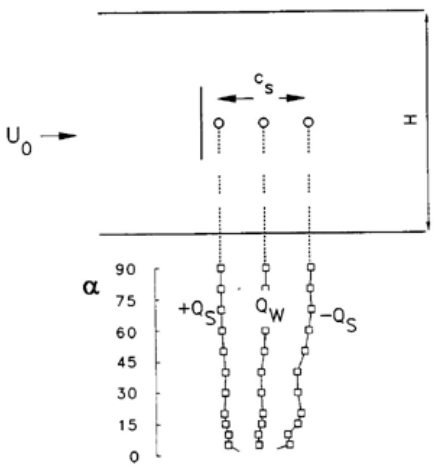

Figure 7 Flow model for the pressure signature method, showing singularity positions for the large model at center tunnel

The attached and separated flow approaches must be combined, in a manner to be determined, to capture the best features of both. Three possibilities will be discussed here.

The first approach is a significant extension of the pressure signature method that adds horseshoe vortices, off-center model capability and the use of model forces to the previous program. Lift effects are first removed from the wall pressure signatures using measured lift and an initial estimate for flow model geometry. The resulting difference signatures, which should now contain only blockage effects, are then treated using conventional pressure signature procedures, which return new singularity positions, source strengths and interference velocities. The original signature is re-analyzed using this new information and the procedure is repeated until the flow model converges. The corresponding 2D procedures are described in detail in [10]. The model shapes implied by these procedures are fully yielding so the method should be well suited to highly separated cases.

The second approach, currently under early development, modifies standard vortex lattice procedures by adding source elements to simulate separation. There are important differences between the boundary conditions used in the two approaches. In its augmented form, described above, the pressure signature approach uses wall pressures and total model forces, but no model surface conditions. The lattice-based approach starts with the attached flow case and model surface boundary conditions, supplements the flow model with sources and adds tunnel boundary data as needed to close the problem uniquely.

The third approach, designated "Maskell III", is a further extension of Maskell's original method, beyond that in [11] and [7], that predicts lift increments. Maskell's original method employs momentum considerations to determine the effective dynamic pressure in a test section for models with extreme, bubble-type separation. In the most-used version, the procedure starts by estimating viscous drag. This involves analyzing the relationship between total uncorrected C_D and uncorrected C_L^2 (see [1]). However, the effective dynamic pressure correction that is found accommodates not only the actual change in dynamic pressure caused by tunnel interference but also an incremental drag, ΔC_D, that corrects for distortion of the separation bubble. Since this distortion occurs at the in-tunnel value of dynamic pressure, correction for it ought to be applied prior to the dynamic pressure correction itself. [11] derives a two-step procedure that achieves this. Recently, [7] has reviewed results for several bluff shapes, showing that over-correction associated with the original method is eliminated by the two-step procedure. The results below explore a new extension that recognizes that a given drag increment is caused by a tunnel induced change to an essentially uniform base pressure. The Maskell III extension considers the upper surface of a fully-stalled wing, at angle of attack α, as a base flow. ΔC_D, which is already available using the

previous procedure, is the horizontal component of a normal-to-wing increment ΔC_N so $\Delta C_N = \Delta C_D/\sin\alpha$. ΔC_L, the vertical component, is given by $\Delta C_L = \Delta C_N \cos\alpha = \Delta C_D/\tan\alpha$. Also, there is an incremental pitching moment correction, ΔC_M, associated with the normal force increment, ΔC_N. ΔC_M is zero if moments are taken about the half-chord point, as in this case, since ΔC_N acts at half-chord.

4 Development of force increment equations for three dimensional flow

In [10], equations are derived for two-dimensional increments ΔC_L, ΔC_D and ΔC_M as products of force or moment coefficients with tunnel induced velocity increments or their gradients. The overall form of the correction, typified by the drag equation, is

$$C_{Dc} = \frac{C_{Du} - \Delta C_D}{(1+\varepsilon)^2}$$

The flow model used involves a three source, three vortex arrangement as for the augmented pressure signature method. The three dimensional analysis below parallels that of [10] but now assumes that the interference velocities cannot be resolved into their constituent parts. This provides a more general form that is not specific to solid-walled wind tunnels. Cancellations between terms, seen analytically in [10], now occur numerically.

The kinematic equations for tunnel induced drag, lift and pitching moment are:

$$\Delta D = \sum_{i=1}^{3}\sum_{j=1}^{6}\left[\rho Q_i b_i u_{ij} - \rho \Gamma_i b_i v_{ij}\right] \quad (1)$$

$$\Delta L = \sum_{i=1}^{3}\sum_{j=1}^{6}\left[+\rho \Gamma_i b_i u_{ij} - \rho Q_i b_i v_{ij}\right] \quad (2)$$

$$\Delta M = \sum_{i=1}^{3}\sum_{j=1}^{6}\left[\rho Q_i b_i u_{ij} - \rho \Gamma_i b_i v_{ij}\right] y_i - \sum_{i=1}^{3}\sum_{j=1}^{6}\left[\rho \Gamma_i b_i u_{ij} - \rho Q_i b_i v_{ij}\right] x_i \quad (3)$$

where u_{ij} and v_{ij}, the axial and normal-to-chord velocities induced by the tunnel wall images of singularity j, act on singularity i, having span b_i. Using the pressure signature flow model, Q_1, Q_2, Q_3 become $+Q_S$, $+Q_W$, $-Q_S$, respectively (Figure 7), having dimensions (L^2/T). Vortex strengths Γ_1, Γ_2, Γ_3 become $+\Delta\Gamma$, $+\Gamma_T$, and $-\Delta\Gamma$, also with dimensions (L^2/T). Normalizing (1) to obtain the incremental drag coefficient gives

$$\Delta C_D = \sum_{i=1}^{3}\sum_{j=1}^{6}\left[\overline{C}_{Dvis_i}\varepsilon_{ij} - \overline{C}_{L_i}\delta_{ij}\right] \quad (4)$$

where the overbars denote effective values of the coefficients, defined by

$$\overline{C}_{L_1} = 2\Delta\Gamma/(U_o c),\ \overline{C}_{L_2} = 2\Gamma_T/(U_o c),\ \overline{C}_{L_3} = -2\Delta\Gamma/(U_o c) \quad (5)$$

$$\overline{C}_{Dvis_1} = 2Q_S/(U_o c),\ \overline{C}_{Dvis_2} = 2Q_W/(U_o c),\ \overline{C}_{Dvis_3} = -2Q_S/(U_o c) \quad (6)$$

The singularity strengths in (4) through (6) may be obtained using the augmented pressure signature method, described above. The use of line source strengths in the above analysis is helpful because the resulting equations closely parallel the corresponding two dimensional results, as in [10]. Conversion from the more familiar point source Q/(UBH) form is straightforward.

If we now assume the use of total values for ε and δ, the j summations may be dropped and

$$\Delta C_D = [\overline{C}_{Dvis_1}\varepsilon_1 + \overline{C}_{Dvis_2}\varepsilon_2 + \overline{C}_{Dvis_3}\varepsilon_3] - [\overline{C}_{L_1}\delta_1 + \overline{C}_{L_2}\delta_2 + \overline{C}_{L_3}\delta_3] \quad (7a)$$

Since $\overline{C}_{L_3} = -\overline{C}_{L_1}$ and $\overline{C}_{Dvis_3} = -\overline{C}_{Dvis_1}$ we obtain

$$\Delta C_D = \overline{C}_{Dvis_2}\varepsilon_2 + \overline{C}_{Dvis_1}(\varepsilon_1 - \varepsilon_3) - \overline{C}_{L_2}\delta_2 - \overline{C}_{L_1}(\delta_1 - \delta_3) \quad (7\ b)$$

Proceeding similarly for ΔC_L and ΔC_M:

$$\Delta C_L = [\,\overline{C}_{L_1}\varepsilon_1 + \overline{C}_{L_2}\varepsilon_2 + \overline{C}_{L_3}\varepsilon_3\,] - [\,\overline{C}_{Dvis_1}\delta_1 + \overline{C}_{Dvis_2}\delta_2 + \overline{C}_{Dvis_3}\delta_3\,] \quad (8\,a)$$

$$= \overline{C}_{L_2}\varepsilon_2 + \overline{C}_{L_1}(\varepsilon_1 - \varepsilon_3) - \overline{C}_{Dvis_2}\delta_2 - \overline{C}_{Dvis_1}(\delta_1 - \delta_3) \quad (8b)$$

$$\Delta C_M = \kappa\,(c_S/2c)\,[\,\overline{C}_{L_1}\varepsilon_1 - \overline{C}_{L_3}\varepsilon_3\,] - \kappa\,(c_S/2c)\,[\overline{C}_{Dvis_1}\delta_1 - \overline{C}_{Dvis_3}\delta_3\,] \quad (9\,a)$$

$$= \kappa\,(c_S/c)\,\overline{C}_{L_1}(\varepsilon_1 + \varepsilon_3)/2 - \kappa\,(c_S/c)\,\overline{C}_{Dvis_1}(\delta_1 + \delta_3)/2 \quad (9\,b)$$

where c_S, the solid blockage source-sink spacing, is as shown in Figure 7. Because the present singularities lie on a horizontal line the y_i terms in (3) do not appear in (9). As in [10], the compensation factor κ is introduced because the singularities in the flow model are arranged horizontally and pitching moments due to horizontal forces cannot be recognized. In the absence of other information, κ is set to unity, implying that ΔC_M is entirely due to lift. Setting κ to unity is also equivalent to a small-model assumption. As shown in the extensive two-dimensional analysis of [10], $(\varepsilon_1-\varepsilon_3)$ and $(\delta_1-\delta_3)$, in (8), can be expressed as x-derivatives. To the same order, $(\varepsilon_1+\varepsilon_3)/2$ and $(\delta_1+\delta_3)/2$, in (9b), may be approximated by ε_2 and δ_2 respectively.

The lead terms in (7b) through (9b) are usually dominant. In another notation (e.g. Equation (19) of [10]) the first term in (7b) is $\varepsilon_W C_{Dvis}$, the effect of the far-downstream sink, $-Q_W$, and its images on the in-tunnel wake source + Q_W. The third term in (7b) represents the thrust caused by tunnel-induced upwash acting on the lifting vortex, Γ_T. This upwash is induced by the trailing vortex system and is absent in two dimensions. The upwash terms would be removed if an axis rotation correction procedure were used. A constant-alpha procedure is therefore essential for consistency if (7b) through (9b) are evaluated in full. The first and third terms in (7b) are gradient effects on solid blockage and pitching moment singularities, respectively. The components of the terms in (8), for lift increment, are at right angles to those in (7). Thus the first term in (8b) becomes the lift increment due to axial flow effects on the lifting vortex. The lead term in (9b) can be identified as the pitching moment increment due to the action of tunnel induced axial velocity on $\pm\Delta\Gamma$. The second term is due to tunnel induced upwash acting on the solid blockage source-sink, $\pm Q_S$.

Evaluation of the interference increments in the context of the augmented pressure signature method is straightforward because the singularities are defined as part of the signature analysis. Lift, drag and pitching moment increments may be computed directly, using equations (5) through (9). This is not an option for the two-variable method and a procedure for evaluating the four singularity strengths Q_W, Q_S, $\Delta\Gamma$ and Γ_T must be found. Three new equations for total force and moment coefficients could be derived, similar to (7) through (9). However, a fourth equation, associated with model/wake thickness, is required for full closure. In principle, Q_W, Γ_T, and $\Delta\Gamma$ could be found from measured forces by considering only direct terms in the new total force equations. However, even with this approximation, the lack of a thickness equation means that Q_S still can not be found without further information. Even though total lift, drag, pitching moment and a full definition of the velocity field are all available, full closure is lacking for the two-variable method.

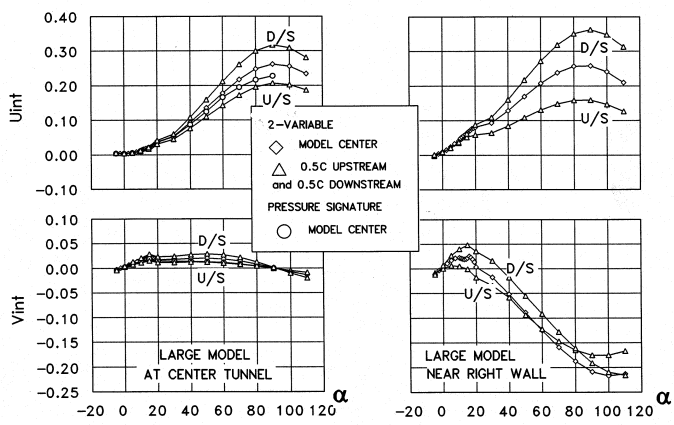

Figure 8 Effect of wall proximity on interference velocities

5 Preliminary results

Model flow environment

Figures 8 and 9 define the flow environment for the largest model (S/C=0.16) at tunnel center and in the near-to-wall configuration. The velocities were calculated at x = - 0.5c, 0 and +0.5c, z = 0 and the appropriate y position, using the two-variable method. Post-stall, moving the model to the near-wall position doubles dU/dX (Figure 9). This is accompanied by large, wall-induced angle of attack (Figure 8). However, dV/dX values are generally lower than dU/dX.

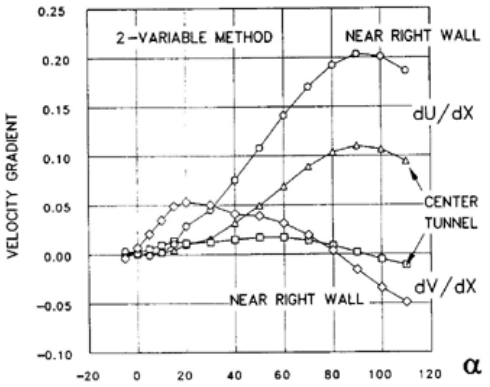

Figure 9 Longitudinal velocity gradients at model location for large model at center tunnel and 0.717c from right wall

Corrections using the Maskell III approach

Figure 10 shows lift and drag increments calculated using the Maskell III method for all four models at tunnel center. By definition, these increments are zero until separation begins. Similar calculations (not shown) reveal little change in either the lift or the drag increments when the model approaches the tunnel wall. This may be due to the fact that this procedure is based only on measured separation drag and has no direct coupling to wall proximity effects.

Figure 11 shows uncorrected C_L and C_D for the largest model at tunnel center (filled circle symbols) and a complete set of fully corrected data (other symbols) using the Maskell III procedure. These corrections were made at constant alpha. The data collapse for the four models is very good.

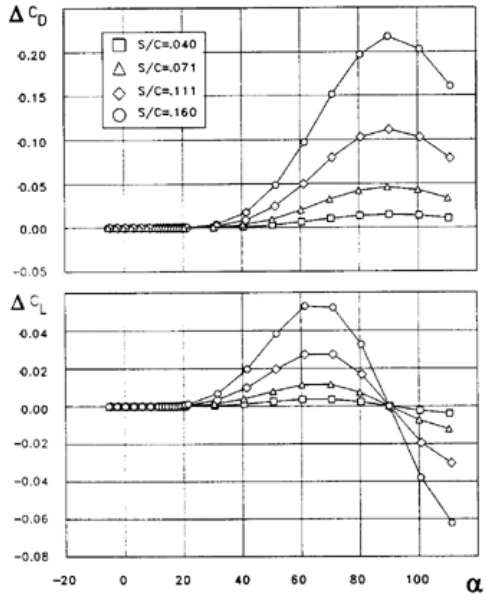

Figure 10 "Maskell III" drag and lift increments with models at tunnel center

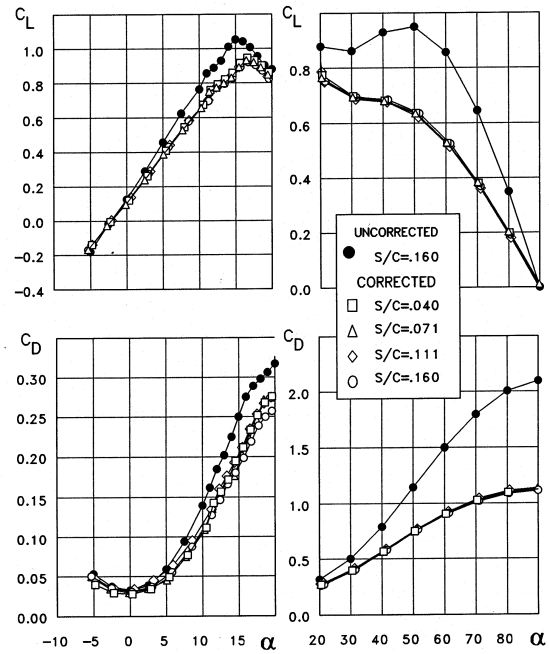

Figure 11 Correction of data using " Maskell III " increments with models at tunnel center

Figure 12 gives the corresponding data with the models near to the right wall, 0.88 model chords from them. The data collapse is again good. It will be noticed, too, that proximity to the right wall increases uncorrected C_{LMAX}. This tendency increases for models in the closest-to-wall condition, 0.717 chords away (not shown).

Somewhat remarkably, bearing in mind the velocity gradients that are present (Figure 9), the corrected C_{LMAX} is somewhat greater than that found at tunnel center. There is more scatter in both uncorrected and corrected C_D data at low incidence. However, the agreement between models at high incidence is extremely good.

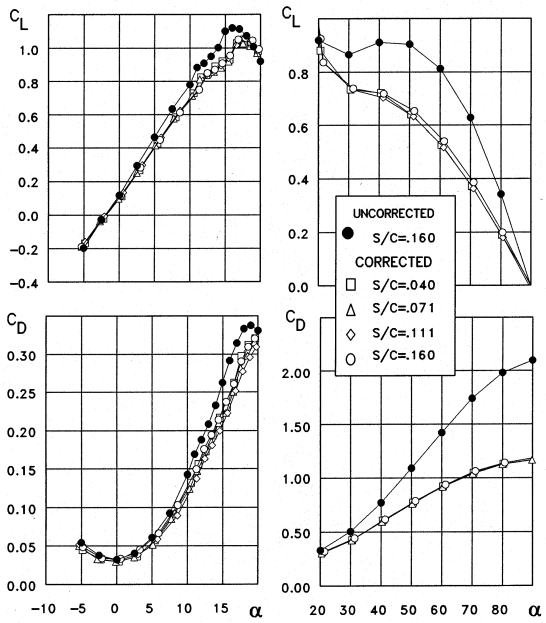

Figure 12 Correction of data using "Maskell III" increments with models 0.88c from the right wall

If viscous drag can be estimated reliably, the extended Maskell method of [7] produces good results and no special information is needed concerning model geometry or wall pressures. However, the present estimates of C_L increments, using Maskell III, rely on knowing that the base of the model is inclined at the model angle of attack. A different angle would be appropriate for a body with a scarfed base, for example. For more complicated shapes, the difficulty of estimating the appropriate base angle could inhibit the use of the Maskell III procedure.

Corrections using the augmented pressure signature method.

Figure 13 shows center-tunnel results using the augmented pressure signature method. The pressure signature opposite to the wing tip (Row 8) was employed, together with lift and pitching moment measurements. The standard asymptote capturing procedure was used. Incremental forces calculated on the six-singularity flow model were corrected at constant angle of attack, as for the Maskell III results.

Up to stall, the corrected results of Figure 13 almost duplicate those obtained using the Maskell III method in Figure 11. Post-stall, the corrected lift data show similar, though not identical trends to the Maskell III results. However, both lift and drag are over-corrected for the larger models at angles above 60 degrees. This has been traced to insufficient downstream signature length. The asymptotic pressure estimates, on which wake source strength is based, are too high and this causes the over-correction. This might be avoided by estimating the viscous drag coefficient by other means, as in [1] for example, and defining the wake source strength directly.

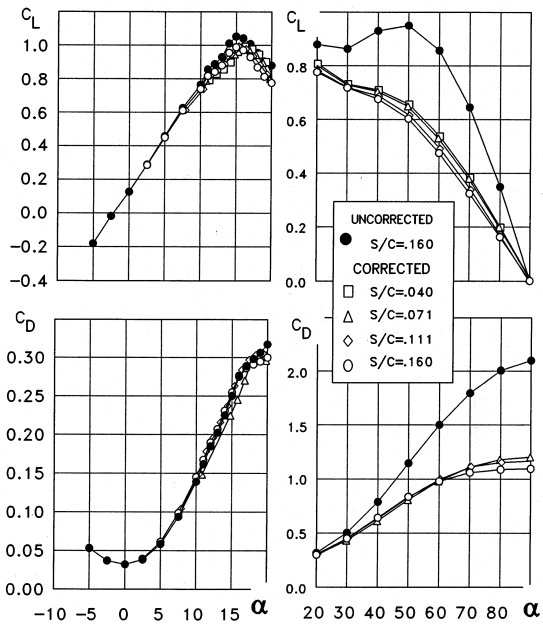

Figure 13 Application of augmented pressure signature corrections to models at Y=0

CORRECTED AFT OF THE MODEL

Figure 14 shows results with each model positioned with its lifting surface 0.88 chords from the right tunnel wall. At angles of attack below 10 degrees the signature iteration sometimes failed to converge. This was traced to signatures that were weak or had ill-defined

peaks. A better choice of orifice row, opposite to the wing's lifting surface (Row 13), would probably have avoided this.

The post-stall drag data in Figure 14 are under corrected and the lift data are grossly over corrected. Calculating forces on the six-singularity flow model, which worked well at center tunnel, failed with the model at off-center locations. An alternative procedure was therefore adopted that calculates tunnel-induced forces at the model center. This change of strategy is discussed in Section 6.

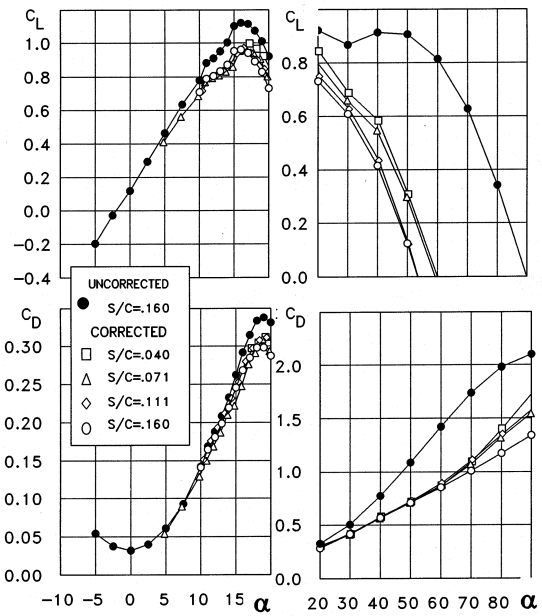

Figure 14
Application of augmented pressure signature corrections with the models 0.88c from the right wall: CORRECTED AFT OF THE MODEL

Figure 15 shows center-tunnel corellations using the new strategy. Pre-stall, the signature-based corrections of Figures 13 and 15 are noticeably smaller than those using the Maskell III approach (see Figure 11) and they exhibit more scatter. Post-stall, the revised corrections are somewhat smaller than for Maskell III. This difference can be traced to thrust produced by vortex image induced upwash acting on the bound vortex. The Maskell III approach has no way of sensing this.

In Figure 16 we see that the previous lift over-correction has been eliminated and the post-stall results for lift agree well with those using the Maskell III approach (Figure 12). The agreement between corrected near-wall and center-tunnel C_{LMAX} in Figure 15 and 16 is remarkably good. The drag correction using the augmented signature approach is again smaller than when using Maskell III, for the reasons described above. The overall correlation among models in Figure 16 is very good.

We now return to the original question of whether near-wall and center-tunnel data can be corrected successfully to a common free air result. Comparing Figures 11 and 12, for the Maskell III procedure, we see differences between corrected center tunnel and corrected near-wall data at stall but there is good agreement otherwise. There is better agreement between center tunnel and near-wall corrected data at stall for the augmented pressure signature method (Figures 15 and 16) and some under-correction for the larger models.

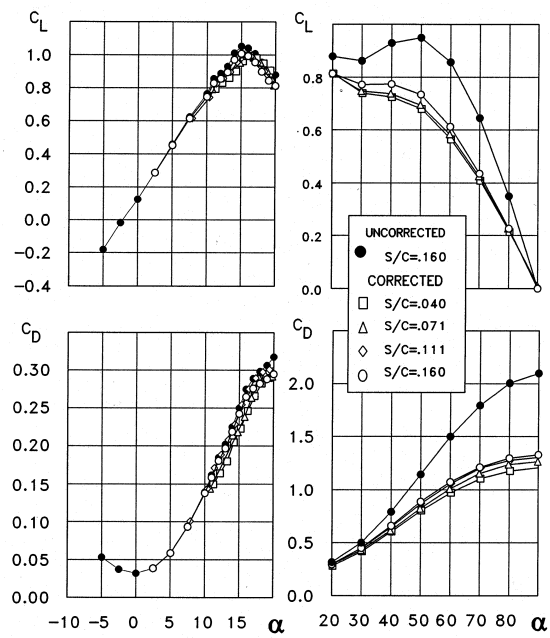

Figure 15
Application of augmented pressure signature corrections to models at tunnel center, CORRECTED AT THE MODEL.

Corrections using the two-variable method

As mentioned in Section 4, the determination of singularity strength, defined in (5) and (6), requires model thickness and other information that is unavailable when using the two-variable method on its own. A first approximation

assumes a small model and invariance under constraint, as in classical theory. Under these assumptions, $\overline{C}_{L2}$ and $\overline{C}_{Dvis2}$ in (5) and (6) become measured lift coefficient and estimated viscous drag coefficient respectively. It is possible to improve this approximation by using in-tunnel velocities for scaling, keeping velocity-times-strength products constant. Strengths $\overline{C}_{L1}$ and $\overline{C}_{L3}$, distance c_S apart, imply a doublet that represents pitching moment coefficient. $\overline{C}_{Dvis1}$ and $\overline{C}_{Dvis3}$, also c_S apart, are equivalent to a solid blockage doublet. The strength of the latter is difficult to estimate for separated flows.

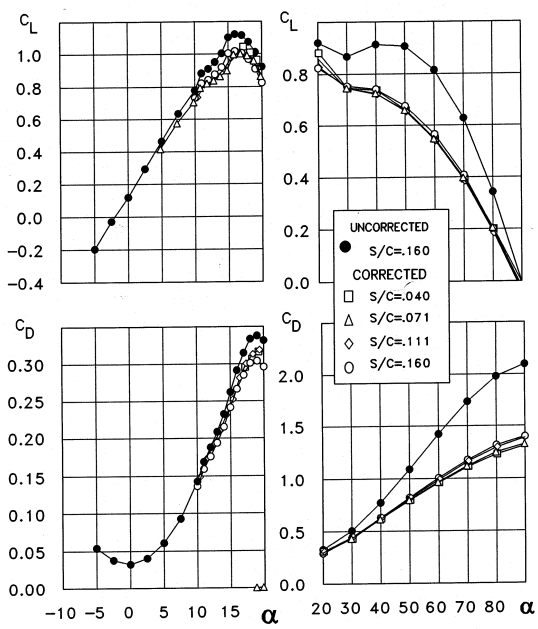

Figure 16
Application of augmented pressure signature corrections with the models 0.88c from the right wall CORRECTED AT THE MODEL

Bearing in mind the findings above, the preferred approach is now to calculate interference velocities and their gradients at the model center, preferably the aerodynamic center. Force calculations for the two variable method are then the same as for the augmented pressure signature method.

The assumption of invariance under constraint is of doubtful value for large models and when tunnel surfaces are approached closely. A hybrid using the two-variable method to generate interference velocities and the pressure signature method to interpret them is clearly a possibility. However, a simple panel procedure, discussed in Section 2, may be preferable because it is less restrictive and is probably simpler to implement. Such a procedure is currently under development.

6 Discussion

The original pressure signature method calculates forces on flow model singularities aft of the model at the locations determined by the signature fitting procedure (Figure 7). This works well for models at tunnel center but fails badly for off-center models. To explain this, predicted interference velocities and the force calculation procedure have been reviewed in depth. Figure 17 shows interference velocities calculated at the wing center plane using the augmented pressure signature method. These compare well with the corresponding two-variable calculations in Figure 18. In another check, it was found that a flow model derived using pressure measurements on Rail 8 predicted the measured wall pressures on Rails 3 and 13 very well. The flow model appears to be working well so the force calculation becomes the prime suspect.

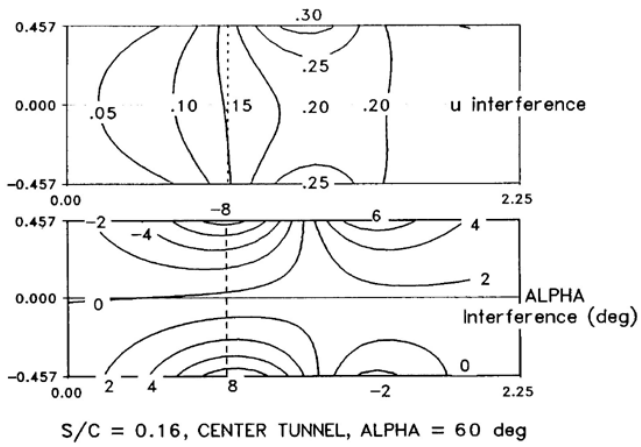

Figure 17 Interference on the wing center plane calculated using the augmented pressure signature method.

It is obvious that the most relevant interference velocities are those at the model itself. Interference velocities increase rapidly aft of the model, where the flow model singularities are located, so over-correction should be expected if forces are calculated on

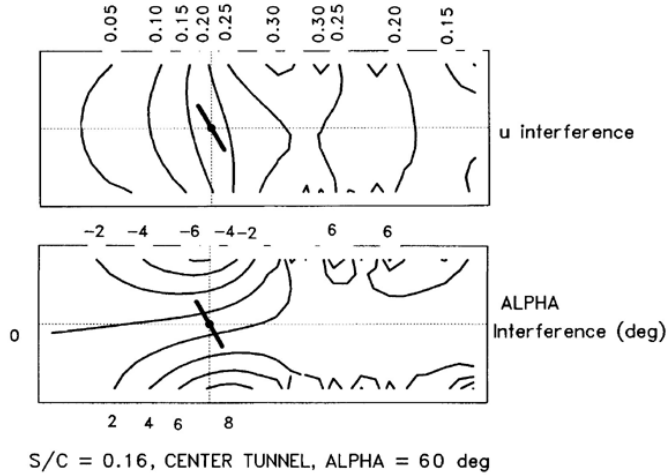

Figure 18 Interference on the wing center plane calculated using the two-variable method wihm2v.

them. This is evidently the cause of the excessive lift corrections seen in Figure 14. The question ought to be "Why do center tunnel cases work?" rather than "Why do off-center cases fail?"

The answer to the first question is that the tunnel center plane possesses unique kinematic properties. As we shall see below, many of the image-induced velocity components are zero at the center plane and some paired force increments cancel. As a result, the lift and drag increment calculations become insensitive to the axial location of the singularities.

Interference velocities are generated at the center plane by bound vortex and line source images (Table 1), by the images of the trailing legs of horseshoe vortices and by the downstream sink, strength $-Q_W$, and its images. Center plane elements experience zero drag for six of the eight interactions shown in Table 1 because the relevant velocities are zero. It may be shown that w is finite for row (5) and u is finite for row (6). However, these velocities act on $\pm\Delta\Gamma$ and $\pm Q_S$ respectively so drag forces oppose one another, giving zero resultant. This completes all the Table 1 drag interactions. Their total drag increment is zero so the position at which drag is calculated becomes moot.

Turning now to the horseshoe vortices, it is apparent that the images of the trailing legs generate only upwash. Only the vortex bound legs can carry drag (actually thrust) and there is

Table 1: Line source and bound vortex image effects for centered models

	Effect of images of	Lift effects	Drag effects	Count
(1)	$\pm\Delta\Gamma$ on Q_W	Net lift but ΔL's cancel for alternate layers	u = 0 so no drag	2
(2)	Q_W on $\pm\Delta\Gamma$		w = 0 so no drag	2
(3)	$\pm Q_S$ on Γ_T	Net lift but ΔL's cancel for alternate layers	w = 0 so no drag	2
(4)	Γ_T on $\pm Q_S$		u = 0 so no drag	2
(5)	$\pm\Delta\Gamma$ on $\pm\Delta\Gamma$	u = 0 so no lift	w finite but drag cancels	4
(6)	$\pm Q_S$ on $\pm Q_S$	w = 0 so no lift	u finite but drag cancels	4
(7)	Γ_T on Γ_T	u = 0 so no lift	w = 0 so no drag	1
(8)	Q_W on Q_W	w = 0 so no lift	u = 0 so no drag	1

no sensitivity to axial location. The downstream sink system produces constant u-velocity throughout the test section and there is net drag only on Q_W. This is usually the major contribution. Again, there is no sensitivity to axial location.

The preceding analysis shows that, with the model on-center, the drag increment is completely insensitive to the axial position at which it is calculated. This explains not only the good results seen in Figure 13 but also the historical success of the pressure signature method when used at center tunnel.

Treating lift interference in the same way, we see that the lift for the 'self' terms, (5) through (8) in Table 1, is zero. Using kinematic analyses similar to those in [10], it may be shown that, in the interaction between $\pm\Delta\Gamma$ and Q_W (rows (1) and (2)), odd-numbered image layers contribute to lift but even layers do not. The same is true for the interactions between $\pm Q_S$ and Γ_T in rows (3) and (4). The lift increment for bound vortex and source interactions will therefore be sensitive to some degree to the position at which it is calculated. The axial velocity induced in the test section by the downstream sinks, acting on the bound vortex, produces most of the net lift increment with the model at center tunnel. As for drag, this means that the x-position of the bound vortex is not an issue. The upwash induced by the images of the trailing vortex system produces no lift on bound vortices so their position is moot. The thrust due to trailer-image-induced upwash on in-tunnel sources is usually small, but noticeable.

The analysis above suggests that lift increments for center tunnel cases may show limited sensitivity to the x-position at which they are calculated. Comparisons among Figures 11, 13 and 15 shows that this is, indeed, the case.

As already indicated, the bottom line is that the success of aft-of-model corrections for models mounted on the tunnel center plane is explained by its unique kinematic properties. Such corrections may fail at off-center locations.

7 Conclusions

New low-speed wind tunnel testing requirements can place a model at a high angle of attack close to a test section roof. The paper discusses the tunnel interference implications of this and demonstrates the occurrence of lift and drag increments caused by tunnel-induced velocity gradients. Pitching moment increments are discussed but are not demonstrated. Theory developed in [10] for evaluating these increments in two dimensional flow is extended here to three dimensions. Three possible correction approaches are discussed. In order of increasing complexity, these comprise:

(a) a further extension of Maskell's blockage correction method, beyond that of [11] and [7], that calculates ΔC_L as well as ΔC_D. This is designated here as "Maskell III".

(b) a significantly augmented version of the pressure signature method, [4,5], that adds horseshoe vortices, off-center model capability and the use of model forces to the previous program.

(c) an approach based on the two-variable method as published in [3]. Means for implementing these methods are discussed.

The theoretical studies were supported by dedicated tests, in an NRC wind tunnel, on a family of four flat plate wings at tunnel center, near to the tunnel "roof" and at intermediate locations. Model planform area ranged from 4% to 16% of tunnel area. An angle of attack range from -5 to 110 degrees was employed in all cases and 240 wall pressures were measured at every data point. Corrected force data for the four models were compared for selected cases and correction procedures. Pitching moment data are not available.

General conclusions

(1) The presence of severe tunnel-induced velocity gradients at the model has been experimentally demonstrated using measured wall pressures with two-variable analysis.

(2) Experiments have demonstrated the presence of tunnel-induced lift increments, as well as drag, under these conditions.

(3) Lift and drag data for models of various sizes were corrected successfully to free air conditions using two different correction methods.

(4) Wall proximity caused an increase in C_{LMAX} as a model's lifting surface approached its image. After correction, however, there was agreement between the near-wall and tunnel center values of C_{LMAX}.

The "Maskell III" method

(5) The method is reliable and simple to use provided that (a) the viscous drag can be extracted successfully from the measured total and (b) the effective slant-angle of the model base is known. The value of the slant angle was obvious for the present flat plate experiments. However, it is anticipated that this requirement will inhibit routine application of the ΔC_L part of the method.

The augmented pressure signature method

(6) The new procedure gives results that agree well with the Maskell III approach for the three smaller models on the tunnel centerline. However, better asymptote capturing procedures are needed for the larger models and far-off-center conditions.

(7) Increasing over-correction occurred as model size increased because the pressure signatures could not be extrapolated to good asymptotes. Alternative procedures have been identified for cases for which the test section is too short. More attention should also be paid to choosing the most appropriate orifice row. Only Row 8 (Figure 3) was employed for the results quoted here.

(8) The flow model determined by the standard, Section 4 procedure produces good estimates of interference velocities but poor interference forces for off-center cases. Over-correction occurs because forces are calculated at the standard locations aft of the model (Figure 7), where the interference velocities are high.

(9) Good results were obtained for off-center cases using the standard procedure to calculate the flow field and then calculating forces at the model location.

(10) The standard formulation works at center tunnel only because this location has special kinematic properties that make the force increments insensitive to the axial location at which they are calculated.

Future work

Plans call for completion of the development of both the augmented pressure signature and the two-variable-plus-panel methods. More complete correlations across the extensive experimental data base are planned.

Acknowledgements

The authors are indebted to Richard Corber and Andrew Stackhouse of NRC for their diligent efforts when performing the experiments described in this paper. Miroslav Mokry, also of NRC, has provided invaluable support throughout the project, particularly concerning the use of his two-variable program, wihm2v.

References

[1] Cooper, K. R, Corber, A Stackhouse, R. An examination of wall-pressure-based correction methods with off-center models in a closed wind tunnel. *National Research Council of Canada* LTR-A-050. April 2000.

[2] Ashill, P. R, Weeks, D. J. A method for determining tunnel wall-interference corrections in solid-wall tunnels from measurements of static pressure at the walls. AGARD-CP-335, pp1.1-1.12. 1982.

[3] Mokry, M. Automation of wall-interference procedures using the C++ object-oriented approach. *AIAA 38th Aerospace Sciences meeting*, Reno, Nev. Paper 2000-0674. Jan 2000.

[4] Hackett, J. E, Wilsden, D. J. Determination of low speed blockage corrections via tunnel wall static pressure measurements. *AGARD Symposium on wind tunnel design and testing techniques*. London, England October 1975. See AGARD CP 174, Paper 22.

[5] Hackett, J. E. Tunnel-induced gradients and their effect on drag. *AIAA Journal* Vol 34 No 12 pp. 2575-2581. Dec 1996.

[6] Maskell, E. G. A theory of blockage effects on bluff bodies and stalled wings in a closed wind tunnel , ARC R&M 3400, November 1963.

[7] Cooper, K. R. Improved blockage corrections for bluff bodies in closed and open wind tunnels. *10th International Conference on Wind Effects on Buildings and Structures*, Sweden, June 1999.

[8] Ewald, B. F. R.(ed). Wind tunnel wall corrections. AGARD-AG-336 pp. 8.22 and 4.30. October 1998.

[9] Browne, L, Katz, J. Application of panel methods to wind tunnel interference corrections. AIAA Paper 90-0007, January 1990.

[10] Hackett, J. E. Drag, lift and pitching moment increments due to wall constraint in a two-dimensional wind tunnel. *AIAA 38th Aerospace sciences meeting*, Reno, Nev. Paper 2000-0672. Jan 2000.

[11] Hackett, J. E., Tunnel-induced Gradients and their Effect on Drag. *Lockheed Engineering Report* LG83ER0108, June 1983 (Revision, Sept. 1994 is available from the author).